

# Sparse Data Machine Learning Integration with Theory, Experiment and Uncertainty Quantification

Process-Structure-Property-  
Performance of Friction Deformation  
Processing

May 2022

Amra Peles  
Scott A. Whalen  
Glenn J. Grant

## DISCLAIMER

This report was prepared as an account of work sponsored by an agency of the United States Government. Neither the United States Government nor any agency thereof, nor Battelle Memorial Institute, nor any of their employees, **makes any warranty, express or implied, or assumes any legal liability or responsibility for the accuracy, completeness, or usefulness of any information, apparatus, product, or process disclosed, or represents that its use would not infringe privately owned rights.** Reference herein to any specific commercial product, process, or service by trade name, trademark, manufacturer, or otherwise does not necessarily constitute or imply its endorsement, recommendation, or favoring by the United States Government or any agency thereof, or Battelle Memorial Institute. The views and opinions of authors expressed herein do not necessarily state or reflect those of the United States Government or any agency thereof.

PACIFIC NORTHWEST NATIONAL LABORATORY  
*operated by*  
BATTELLE  
*for the*  
UNITED STATES DEPARTMENT OF ENERGY  
*under Contract DE-AC05-76RL01830*

Printed in the United States of America

Available to DOE and DOE contractors from  
the Office of Scientific and Technical  
Information,  
P.O. Box 62, Oak Ridge, TN 37831-0062  
[www.osti.gov](http://www.osti.gov)  
ph: (865) 576-8401  
fox: (865) 576-5728  
email: [reports@osti.gov](mailto:reports@osti.gov)

Available to the public from the National Technical Information Service  
5301 Shawnee Rd., Alexandria, VA 22312  
ph: (800) 553-NTIS (6847)  
or (703) 605-6000  
email: [info@ntis.gov](mailto:info@ntis.gov)  
Online ordering: <http://www.ntis.gov>

# **Sparse Data Machine Learning Integration with Theory, Experiment and Uncertainty Quantification**

Process-Structure-Property-Performance of Friction Deformation Processing

May 2022

Amra Peles  
Scott A. Whalen  
Glenn J. Grant

Prepared for  
the U.S. Department of Energy  
under Contract DE-AC05-76RL01830

Pacific Northwest National Laboratory  
Richland, Washington 99354

## Abstract

Computer vision and deep learning tools that advance the ability to establish processing-structure-property-performance (PSPP) relations are presented. The Bayesian binning method for image segmentation enables quantitative analysis of microstructural features in an automated way, while the analysis of shapes and relative orientation of these features reveals local deformation maps indicative of both, material flow and residual stresses due to materials processing. The deep learning method leads to the previous knowledge agnostic mapping of empirically observed microstructural zones in friction stir welding (FSW) process and synthetic microstructure generation capability that is statistically equivalent to experimentally collected data.

## Summary

The processing–structure–properties–performance (PSPP) relationship is a guiding principle for development and improvement of advanced materials, processes and manufacture. The specific goal of this project was to ascertain processing–structure–properties–performance relationship via *mechanistic understanding* and *merit descriptors* of the well performing friction-deformation alloy processing of solid materials coupled with exploitation of *sparse data machine learning* techniques.

Advanced materials processing and/or manufacturing processes allow for tuning of many parameters that control the end properties of fabricated materials and components, which in turn are driven by multiple, complex and convoluted scientific laws at various spatial and temporal hierarchies with often unknown figures of merit. Any predictive PSPP capability that relies on intuition and trial and error becomes an intractable problem without the proposed holistic materials informatics approach.

The material processing experiments in laboratory are essential for all research. The capability developed through this research will move us from the trial and error and subject matter expert input in designing the experiments to achieve our goals to the ability to maximize information about materials properties based on a bare minimum of processing runs and model discriminators. Developed methods and tools will be transferable to other development cases.

## Acknowledgments

This research was supported by the Energy and Environmental Directorate (EED) Mission Seed, under the Laboratory Directed Research and Development (LDRD) Program at Pacific Northwest National Laboratory (PNNL). PNNL is a multi-program national laboratory operated for the U.S. Department of Energy (DOE) by Battelle Memorial Institute under Contract No. DE-AC05-76RL01830.

## Contents

Abstract.....	ii
Summary .....	iii
Acknowledgments.....	iv
Acronyms and Abbreviations.....	<b>Error! Bookmark not defined.</b>
1.0 Introduction.....	1
2.0 Methods and Results.....	3
2.1 Friction stir welding experimental details.....	3
2.2 Computer Vision .....	3
2.3 Machine Learning .....	7
2.3.1 Data Preprocessing .....	7
2.3.2 Semi-supervised Generative Adversarial Network.....	9
2.3.3 s-GAN predictions .....	12
3.0 Conclusions.....	14
4.0 References.....	15
Appendix A – Supplementary Information .....	A.1

## 1.0 Introduction

Materials Processing-Structure-Property-Performance (PSPP) relationships are at the center of efforts to develop fit-for-purpose materials and advance the technology. Establishing these relationships is the main challenge of materials research and discovery, whether it is directed to understanding underlying physics of existing materials or to unlocking the potential of new materials and materials processing [1, 2, 3, 4].

Friction stir welding (FSW) is one such solid state materials processing method that joins materials parts together [5, 6, 7] The idea behind the process is rather simple: a non-consumable rotating tool is plunged into and advanced through abutment of parent materials. The tool consists of a shoulder and a pin, as depicted in Figure 1. After plunging, the tool shoulder motion generates frictional heat causing the materials to soften and deform plastically while the advancing rotating pin is stirring softened materials together. The result is formation of a solid-state bonds and materials joining.

Reducing a risk of failure at the joints is a major challenge in the engineering design. The points of failure in the joints are predominantly due to the internal and external stresses placed on the joints and due to the loss of improved microstructural features of advanced alloys when subjected to high temperatures and high plastic deformation in joining processes [8, 9]. The FSW impact on the microstructure formed at the joints is significant. Microstructural features contain key information about both, processing history and future performance. Quantifying the changes in microstructure and distribution of local (residual) stresses at the FSW joints is of paramount importance to enhance product design functionality based on material specific properties.

In the past, methods have focused on quantitative characterization and mathematical representation of microstructure geometric features, such as grains, voids, precipitates, and dislocations. Methods focused on finding amounts, numbers, and sizes of these features [10, 11] include the segmentation of digital micrographs [12] and the two-point statistics analysis [13]. The analysis has been chiefly focused on the individual representative image and interpretation of microstructural features. However, numerous challenges remained due to the complex stochastic nature of microscopic images, as well as sensitivities of these microstructure images to local changes in temperature and plastic deformation stresses. Recently, deep learning techniques have been tested as to address these challenges [4, 14, 15, 16, 17].

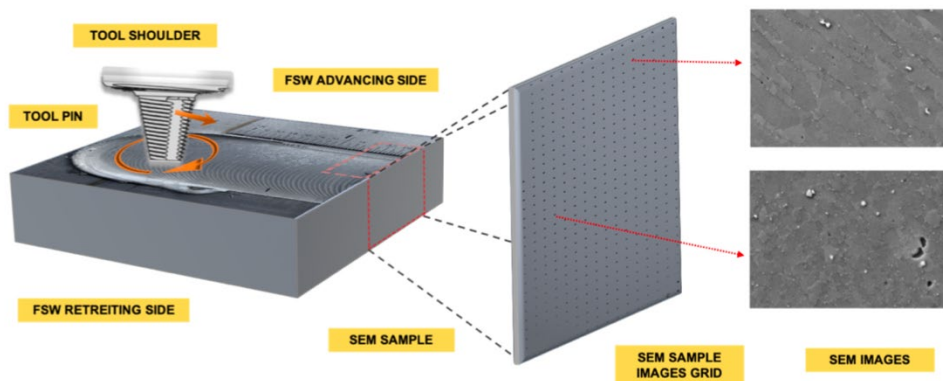


Figure 1 Illustration of FSW experimental set up and SEM images data acquisition strategy. The FSW tool geometry is shown on the top of welded sample with arrows showing its rotational and translation direction.

We present a systematic approach, agnostic to prior knowledge, for identifying different FSW processing zones and microstructure salient stress features by harnessing power of deep learning

and newly developed computer vision analyses. We apply our approach to experimentally acquired scanning electron microscopy (SEM) image data and concurrently generated synthetic and statistically equivalent images. The integration of machine learning with materials research creates new avenues for addressing problems in experimental and theoretical materials science [18].

To study microstructural features imparted by the FSW processing we performed (a) the FSW process to form AA7175 joining with two sets of processing parameters to keep a shoulder temperature at 425 °C and 500 °C, (b) SEM data acquisition at the cross sectional area of the weld, (c) electron dispersive spectroscopy (EDS) for chemical composition insights, (d) a computer vision analysis to quantify most prominent microscopic features and identify local stresses in material due to processing, and (e) a machine learning method that leads to the identification of unique zones with distinct microstructural features.

## 2.0 Methods and Results

### 2.1 Friction stir welding experimental details

The material used in this study is AA7175-T79 aluminum alloy. AA7175-T79 was chosen because its balanced tensile strength, stress corrosion resistance, fracture toughness, and its significance in aerospace and automotive applications. The commercially available 1.1-inch-thick metal sheets were joined using the friction stir welding method with set of welding parameters that led to the temperatures at the FSW tool shoulder of 425 °C and 500 °C.

The FSW tool consists of convex shoulder (36 mm diameter) and conical pin (17.3 mm diameter near shoulder and 8.5° taper angle). The shoulder and pin were featured with three scrolls (9 mm pitch machined with 2 mm diameter ball end mill) and threads (1.42 mm pitch with 0.76mm depth machined). The pin thread was also interrupted with three flats having the machined depth of 1.2 mm. All the welds were performed using temperature-controlled algorithm by modulating the spindle torque of the FSW machine at the Pacific Northwest National Laboratory [27]. Therefore, the tool rotational speed was a response variable which was typically ranging within 70±5 RPM and 260±10 RPM to maintain the commanded shoulder temperature of 425°C and 500°C, respectively. In addition, the tool geometric configurations at a constant 1.5° tool tilt angle facilitate similar shoulder contact condition with commanded forge force (in the vertical direction) of 66.7 kN and 62.3 kN during the FSW processing at 425°C and 500°C shoulder temperatures. The welding speed for this study was kept constant at 76.2 mm/min. The joined plates were cut by water jet to obtain the cross sections of welded samples. We avoided a band saw method to prevent introduction of heat that could have an impact on the final microstructure.

#### *Scanning Electron Microscopy (SEM) and Energy Dispersive X-ray Spectroscopy (EDS)*

The SEM is excellent method for characterization of alloy microstructures, because the necessary sample preparation and image acquisition are relatively quick and simple [19]. The weld cross section specimens were initially polished in a Struers Tegramin-30 semi-automated polisher by grit SiC paper using water as a lubricant, followed by increasingly fine DiaDuo-2 water-based diamond suspension grind with decreasing amount of pressure. In the next step, samples were polished with Struers OP-S Colloidal Silica solution (0.25 micron), followed by a vibratory polisher with a blue colloidal silica solution (0.08 micron). Samples were subsequently rinsed with water, scrubbed with cotton ball, sprayed with ethanol, and dried with compressed air between all steps. The SEM images were acquired on the grid on the samples as depicted in Figure 1. Electron-excited X-ray microanalysis was performed in the scanning electron microscope with energy-dispersive X-ray spectrometry (EDS) on a representative SEM sample to gain insights in the elemental constituents of prominent secondary (intermetallic) phases features observed on all the images. For the reference, the chemical composition of AA7175 alloy is given in the Table 1.

**Table 1 AA7175 alloy chemical composition**

Elements	Si	Fe	Cu	Mn	Mg	Cr	Zn	Ti	Other	Al
Weight %	0.15	0.2	1.2 -2.0	0.1	2.1 – 2.0	0.18 – 0.28	5.1 – 6.1	0.1	3 x 0.5	rest

### 2.2 Computer Vision

Computer vision aims to create algorithmic tools that can process, analyze, and draw conclusions from visual data. The SEM visual data contains the structural information in a form of point by point (i.e., pixel by pixel) strength of the secondary electrons signal. The secondary electrons are

knocked out by the focused beam of primary electrons raster over the surface of the specimen. Our implementation of computer vision enables systematic and consistent examination and extraction of local morphologies of most prominent features in images. We use this information to quantitatively interpret material flow and residual stresses across the FSW processed cross section. The data collection workflow and strategy are depicted in Figure 1.

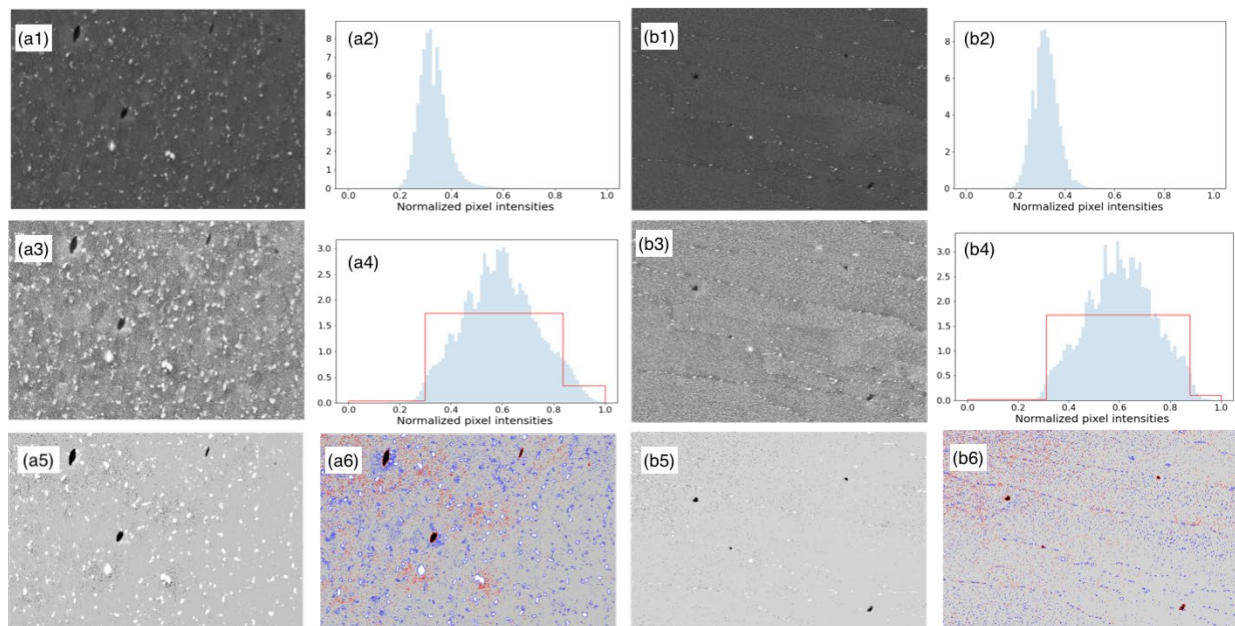


Figure 2 SEM image data processing to extract most prominent features indicative of material flow and distribution of residual stresses. a and b are 425°C and 500°C representative samples. 1. Raw images 2. Raw image histograms 3. Exposure adjusted pre-processed images 4. Histograms of pre-processed images in blue and Bayesian non-uniform three bin histogram 5. The watershed images 6. Images delineating contours about bright phases in blue and dark phases in red.

Figure 2 illustrates steps in data pre-processing and computer vision approach to extract most prominent features for two example samples, obtained at 425°C and 500°C, respectively. The raw data images of the two samples are shown in panels (a1) and (b1), while raw image histograms are shown in panels (a2) and (b2), respectively. The raw images are pre-processed to enhance exposure by setting the gamma exposure parameter for each image at the value corresponding to the maximum of its histogram and by subsequent equalization of exposure using the adaptive histogram method. The processed images are shown in panels (a3) and (b3), and their histograms in panels (a4) and (b4), respectively. To separate visibly prominent features at the tails of pixel intensity histograms, we use an optimal non-uniform binning of image intensity data based on Bayesian method [20]. The bins are shown in red lines in panels (a4) and (b4), and overlaid with conventional uniform binned image histogram shown in blue. This is in contrast with the known watershed methods [21, 22], which use arbitrary cutoff to group similar features. The edges of middle bin in Bayesian histogram are used in a watershed method that leads to the zones (white, black, and light gray) shown in panels (a5) and (b5). We process these images using computer vision contours fitting method. The contours of white features are shown in blue and contours of black features in red in panels (a6) and (b6) in Figure 2. The advantage of our systematic and image specific method that uses Bayesian bins segmentation is the ability to automate analysis over the whole data set (thousands of images). Furthermore, with information about each image contour, we can proceed to quantify number, sizes, and shapes of these

features. For each white feature contour, with area bigger than  $0.25 \mu\text{m}^2$  (to exclude possible colloidal silica particle that may remain after polishing), and each black feature contour with at least 6 points, we compute the feature aspect ratio by fitting a line through data, computing a line perpendicular to it, and determining the contour dimensions along these directions. The aspect ratio is computed as ratio of longer to shorter dimension (a spherical feature having an aspect ratio of 1). Next, the angle of longer dimension with the edge of the image is computed. An average of both, aspect ratios and angles, was computed for every image to examine if feature correlations with material flow or residual stresses is contained in these salient features. Assuming that differences in aspect ratios and orientation of secondary phases are caused by the plastic deformation imparted by the FSW tool motion, we create the distribution of deformation field for the  $425^\circ\text{C}$  sample as shown in Figure 3a. The directions of arrows in Figure 3a correspond to the average angles for each image in the grid and the arrow lengths correspond to each white feature aspect ratio. Figure 3b and 3c shows the stress field for the  $500^\circ\text{C}$  sample for data grid at the center of the weld and close to the tool shoulder. Since  $425^\circ\text{C}$  sample grid was taken over the whole half of the advancing side cross section, careful examination of Figure 3a and comparison with the tool shape shown in Figure 1, indicates that the deformation in microstructural features is consistent with intuitively expected material flow and local residual stresses. The data for  $500^\circ\text{C}$  sample were collected at the fragments of the FSW cross section. Figure 3b shows the deformation field influenced by the tool shoulder while Figure 3c shows the change in the deformation field at the edge of the tool. This unique insight into the material flow characteristics is of practical importance to for optimal tool design and to obtain high structural efficiency welds [6].

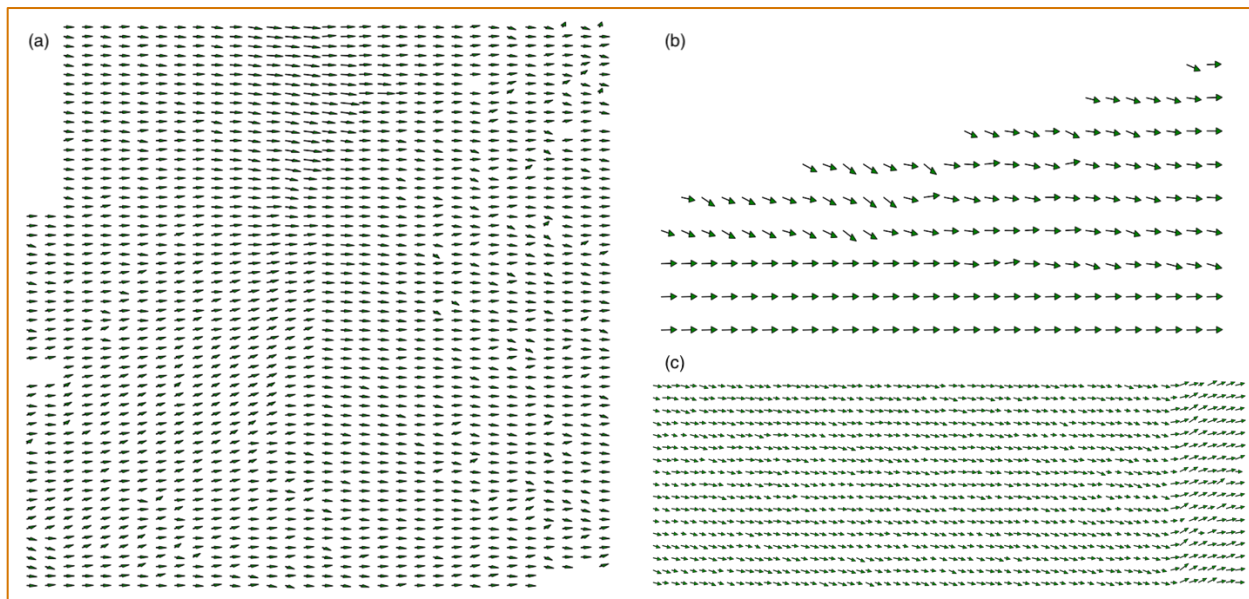


Figure 3 Deformation field extracted via computer vision from the morphology and orientation of bright secondary phase plotted over the grid of points images were collected. A  $425^\circ\text{C}$  image grid, b.  $500^\circ\text{C}$  close to shoulder image grid, c.  $500^\circ\text{C}$  center of weld image grid.

The chemical composition of these most prominent features is examined using the EDS technique.

Figure 5(a) shows EDS elemental analysis of the boxed region in Figure 5(b). In comparison with the alloy matrix, a type brighter in color than the matrix and a type darker in color than the matrix

are distinguished as bright and dark particulates. The bright particulates contain Al, Cu, Fe as primary elements while dark particulates have Zn, Si and Mg as major elements along with a “small” amount of oxygen. Figure 5(c) depicts the image segmentation used to quantify size and shape of these particulate features at the surface of the sample. The dark and bright metallic secondary phases are identified in green and violet by the Bayesian bins method, filtering out features with surface area less than  $0.25\mu\text{m}^2$ . The smaller secondary phase particulates are congregated, and they delineate grains along the grain boundaries. They are shown in red and blue in Figure 5(c), bordering the grains of matrix aluminum alloy.

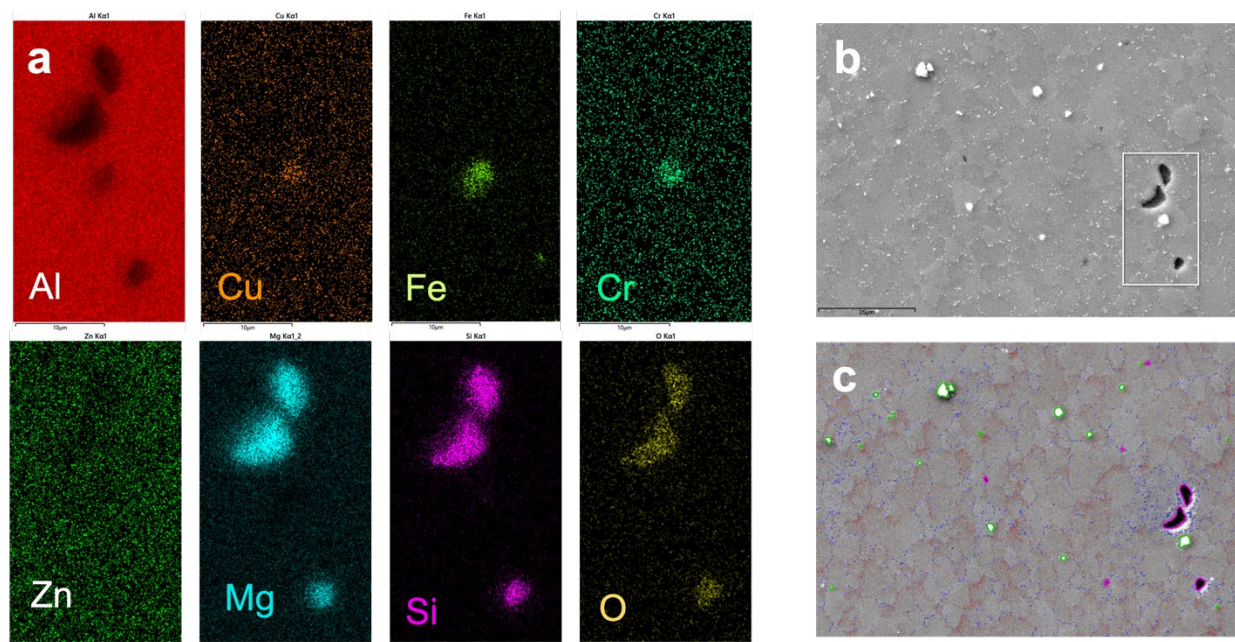


Figure 4 (a) EDS chemical composition analysis (b) the focus boxed area for the EDS analysis (c) The Bayesian method extracted bright and dark particulates

Table 2 summarizes numbers of particulates normalized per  $1\text{ nm}^2$  and the fraction of total surface of all images they cover for both processing temperatures. Figure 5 shows the distribution of particles sizes with respect to their computed sizes. The number of bright particulates is larger at the higher processing temperature and the area covered by bright particulates is more than doubled at  $500^\circ\text{C}$  compared to  $425^\circ\text{C}$  processing temperature. The number of dark particulates is also larger at the higher processing temperature while the total area covered is comparable between two processing conditions.

**Table 2 Summary of quantitative analysis of prominent dark and bright features for  $425^\circ\text{C}$  and  $500^\circ\text{C}$  samples.**

Sample Processing Temperature	Particulate	Number of particulates per $1\text{ nm}^2$	Particulate area (% of total sample area)
$425^\circ\text{C}$	Dark	787.5	0.099
$425^\circ\text{C}$	Bright	23661	0.365
$500^\circ\text{C}$	Dark	1466.7	0.082
$500^\circ\text{C}$	Bright	38731	0.852

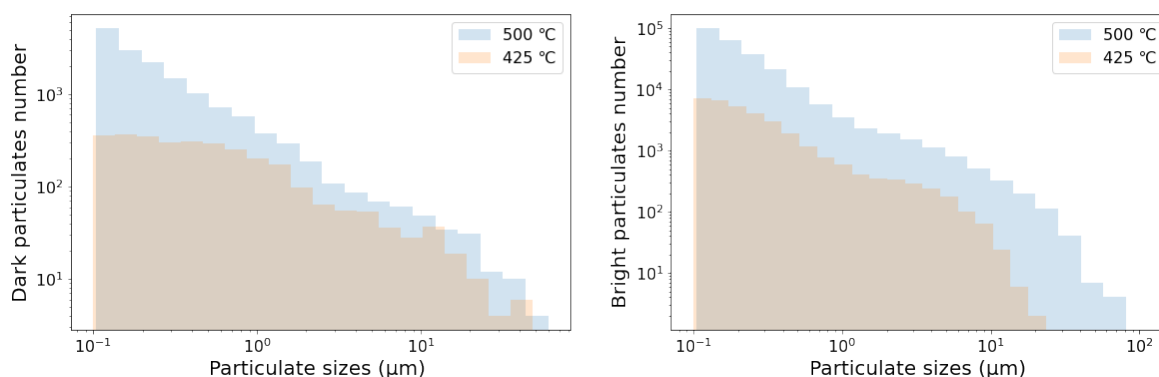


Figure 5 Log-log histogram of the (a) dark parrticulates andd (b) bright particulates distribution with respect to their sizes.

## 2.3 Machine Learning

### 2.3.1 Data Preprocessing

Figure 1 illustrates SEM data collection strategy at the cross section of FSW samples. The size compressed raw data, as collected, is provided in the supplementary material. The data for the 425 °C sample were collected over uniform grid of points at the advancing side of FSW cross section, while the data for the 500 °C sample were collected on a grid at the center of sample and close to the FSW shoulder area. Upon manual inspection, seven raw images were removed from 425 °C data set due to obvious SEM apparatus problems, while 500 °C raw data set was used in its entirety. Overall, image quality with respect to focus, contrast, and detail in raw data, required some image augmentation to improve image exposure and contrast. The SEM collected raw data images have thre identical channels that were converted to gray scale images, without loss of information. The data set for machine learning was formed by extracting the 512 by 512 pixels images from raw data images without overlap. Intensities of these images were rescaled in 2-98% range to enhance image contrast and the images were resized subsequently to 256 by 256 pixels. The final machine learning input data sets had 5,544 images for the 425 °C sample and 2540 images for the 500 °C sample. Visual inspection of both data sets lead to identification of distinct microstructural features and textures as depicted in Figure 6 and Figure 7. Five distinct classes of images in the 425 °C data set were singled out, while only two classes were visually distinct in the 500 °C data set. We have annotated up to 60 representative images in each class for both data sets. The data annotation was done by randomly selecting images from data sets and assigning the class labels manually based on the image similarity to classes depicted in Figure 6 and Figure 7. Altogether, 5.4% and 4.7% of data in 425 °C and 500 °C data sets were labeled, respectively.

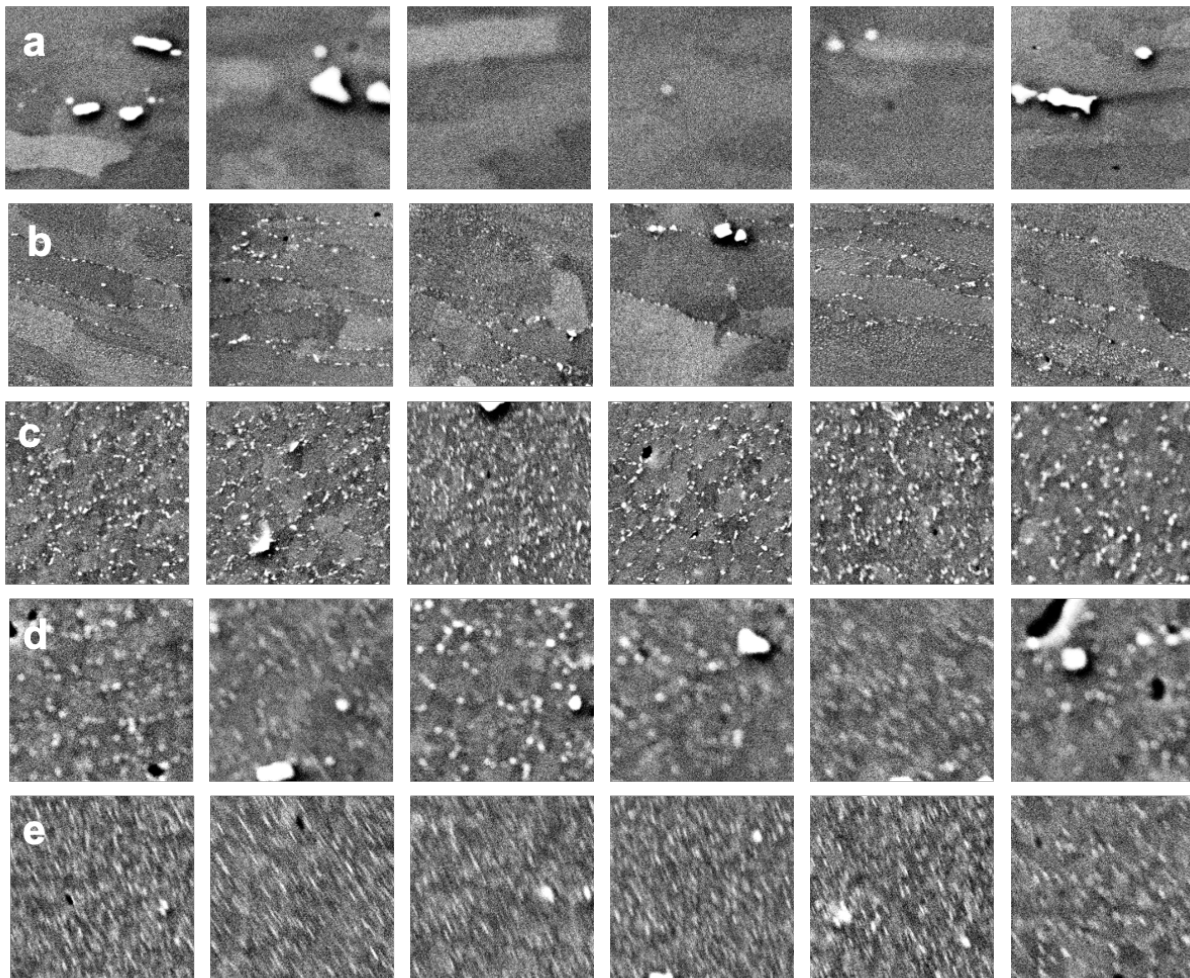


Figure 6 Example images showing morphological differences among SEM data sampled on the grid of 425 °C processes alloy

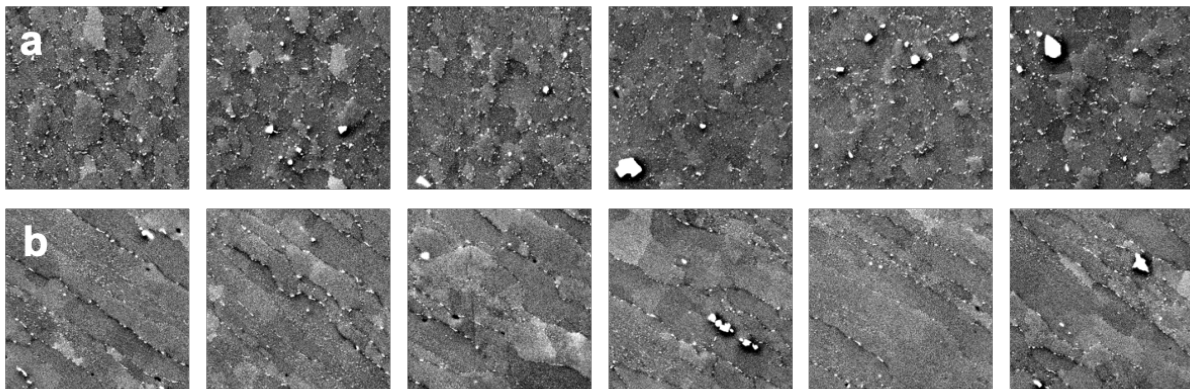


Figure 7 Example images showing morphological differences among SEM data sampled on the grid of 500 °C processes alloy

### 2.3.2 Semi-supervised Generative Adversarial Network

Semi-supervised generative adversarial network (s-GAN) model [23, 24] was chosen to map out empirically suggested FSW zones reported in [5, 6]. The model was chosen to address both, a modest size of unlabeled data set and a small number of manually labeled examples. Our s-GAN model takes advantage of unlabeled data to learn image features and train an image generator model in an unsupervised manner via a discriminator model. The unsupervised discriminator is binary classifier trained to distinguish examples of data from dataset from those generated by the generator model. A classifier model is simultaneously trained to predict a class label of a real image via supervised discriminator model [25, 26]. The model is illustrated in Figure 8, and model architecture details are included in supplementary material (Figure 13).

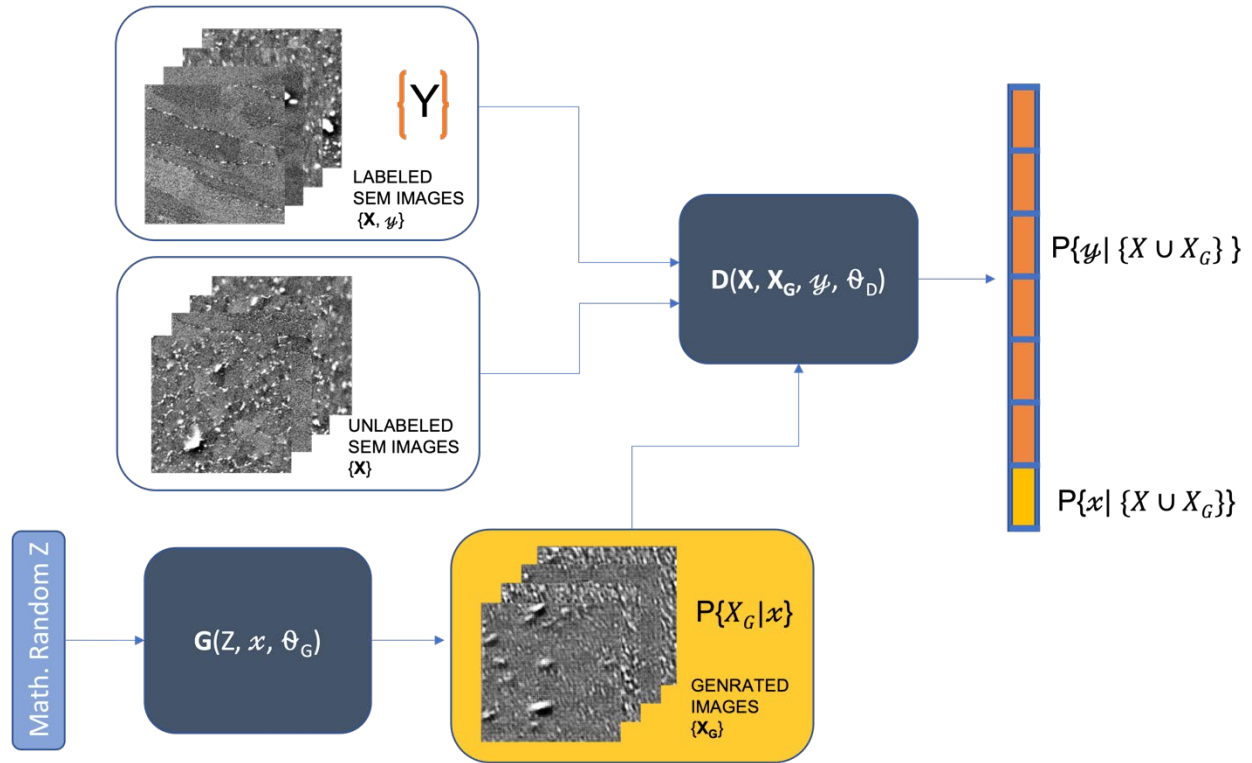


Figure 8. An illustration of the classifier model used in this work.

Generative modeling has been proven to be a good strategy to augment small or missing-data data sets with synthetic data to improve deep neural networks model performance [16, 23]. The generative model in our study is a convolutional neural network (CNN) model  $G(Z, x, \theta_G)$ . The model function  $G(Z, x, \theta_G)$  takes  $Z$ , a vector of arbitrary dimension with random values, as an input feature and it generates plausible microstructure example features  $X_G$ . It is conditioned to learn a probability  $P(X|x)$  of microstructure features  $X$  ( $X_G$ ) given its class  $x$  (real or generated image) through updates of model parameters  $\theta_G$  by optimizing the cost function:

$$J(\theta) = -\frac{1}{m} \sum_{i=1}^m [y^{(i)} \log(G(X^{(i)}, \theta)) + (1 - y^{(i)}) \log(1 - G(X^{(i)}, \theta))]$$

The SEM microstructure samples  $X$ , drawn from the labeled and unlabeled data set, as well as generated images  $X_G$  are fed into a discriminator model  $D(X, X_G, y, \theta_D)$ . The discriminator model is also a CNN. It combines two classifiers. One is conditioned to learn likelihood  $P(x | \{X \cup X_G\})$  that given set of learned features are either from SEM images dataset or generated by generator. The other classifier is conditioned to learn likelihood  $P(y | \{X \cup X_G\})$  that the image belongs to one of  $\{y\}$  classes. The  $P(x | \{X \cup X_G\})$  probabilities are passed as feedback to generator to improve feature learning and generate more realistic images.

The images created by the generator model grouped into the classes  $\{y\}$  are illustrated in the Figure 9 for the 425 °C sample and Figure 10 for 500 °C sample. The figures show images that may not be the highest probability for class results to illustrate the specific features that G model is learning.

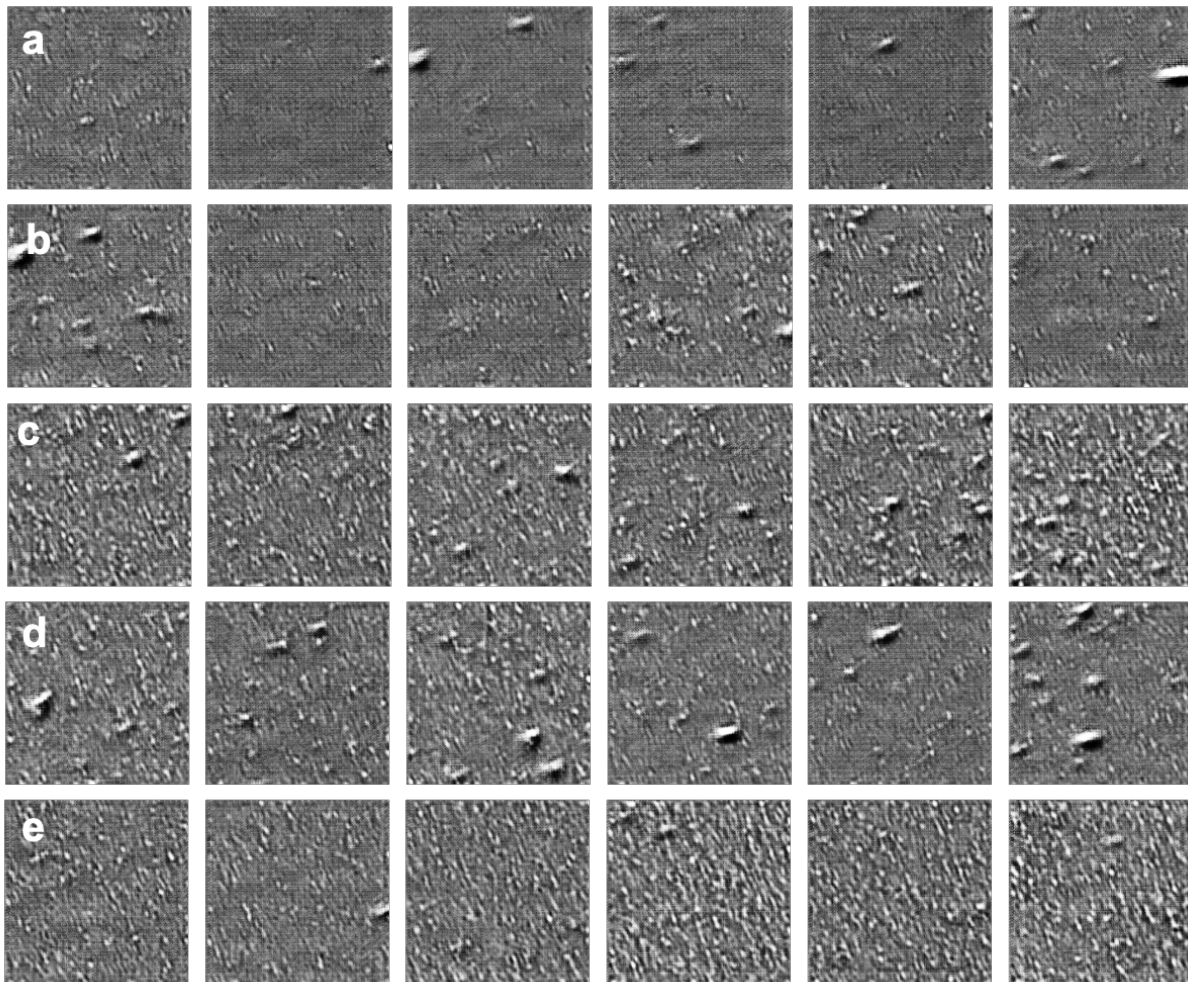


Figure 9 Generated images showing learned morphological features corresponding to labeled classes for SEM data sampled on the grid of 425 °C processes alloy shown in Figure 6.

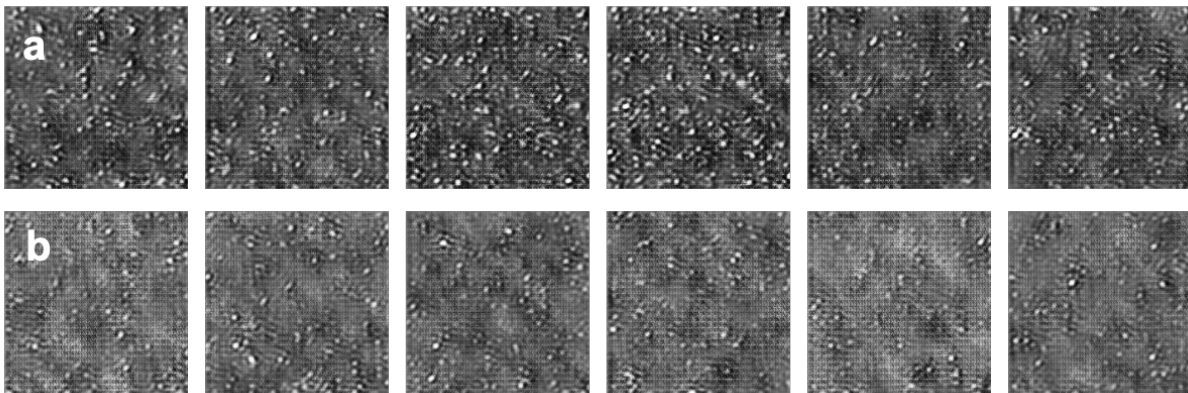


Figure 10 Generated images showing learned morphological features corresponding to labeled classes for SEM data sampled on the grid of 500 °C processes alloy shown in Figure 7.

Semi supervised GAN models are difficult to train due to concurrent optimization of multiple cost functions. The performance of trained models is shown in Figure 11. The cost functions of these models are converging to constant values due to the adversarial nature of generator and discriminator models, while the cost function of the classifier is converging to zero.

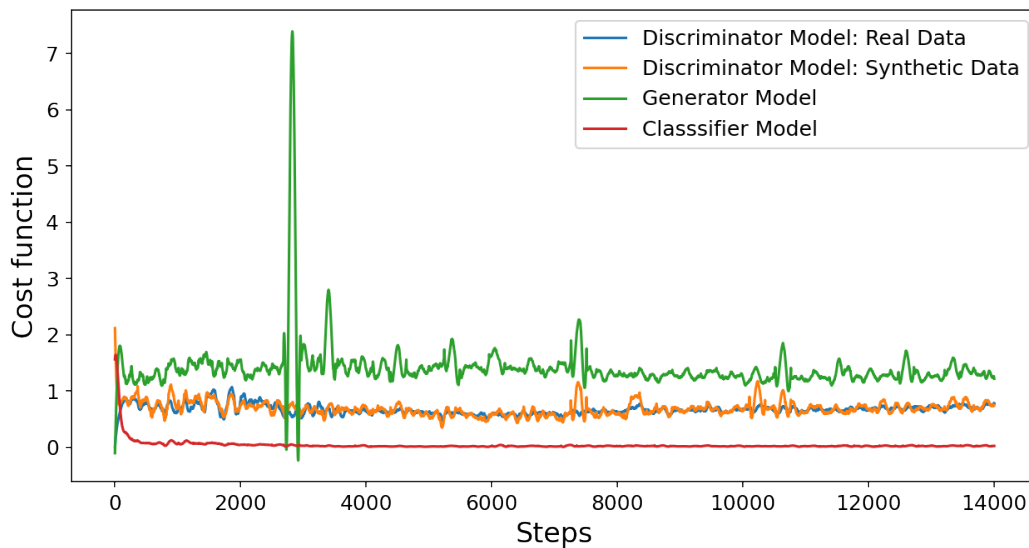


Figure 11 The models performance as the convergence of cost functions with the progression of model training.

The model accuracy with respect to the size of labeled data is shown in Table 3. The model ability to predict the class of an image increases with increasing size of the labeled dataset.

**Table 3 The prediction of image class accuracy with respect to varying size of labeled data.**

Labeled data (% of all data set)	Accuracy of Classifier (%)	Data Set (classes)
1.35	84.0	425 °C (5)
2.7	90.3	425 °C (5)
5.4	92.5	425 °C (5)
2.8	97.2	500 °C (2)
5.5	98.1	500 °C (2)

### 2.3.3 s-GAN predictions

We use trained models to predict classes of images in the unlabeled data set. For illustration, Figure 12 shows the color-coded predicted classes for images assembled in the same grid as in the one where SEM data were acquired. The white, green, red, blue, and magenta in Figure 12a correspond to the classes of images selected to resemble *a*, *b*, *c*, *d*, and *e* microstructural features presented in Figure 6 for 425 °C processed sample. The green and red in Figure 12b correspond to the classes selected to resemble images shown in *a* and *b* in Figure 7 for 500 °C processed sample. The details of the two grids are shown in the supplementary material section (Figure 14 and Figure 15).

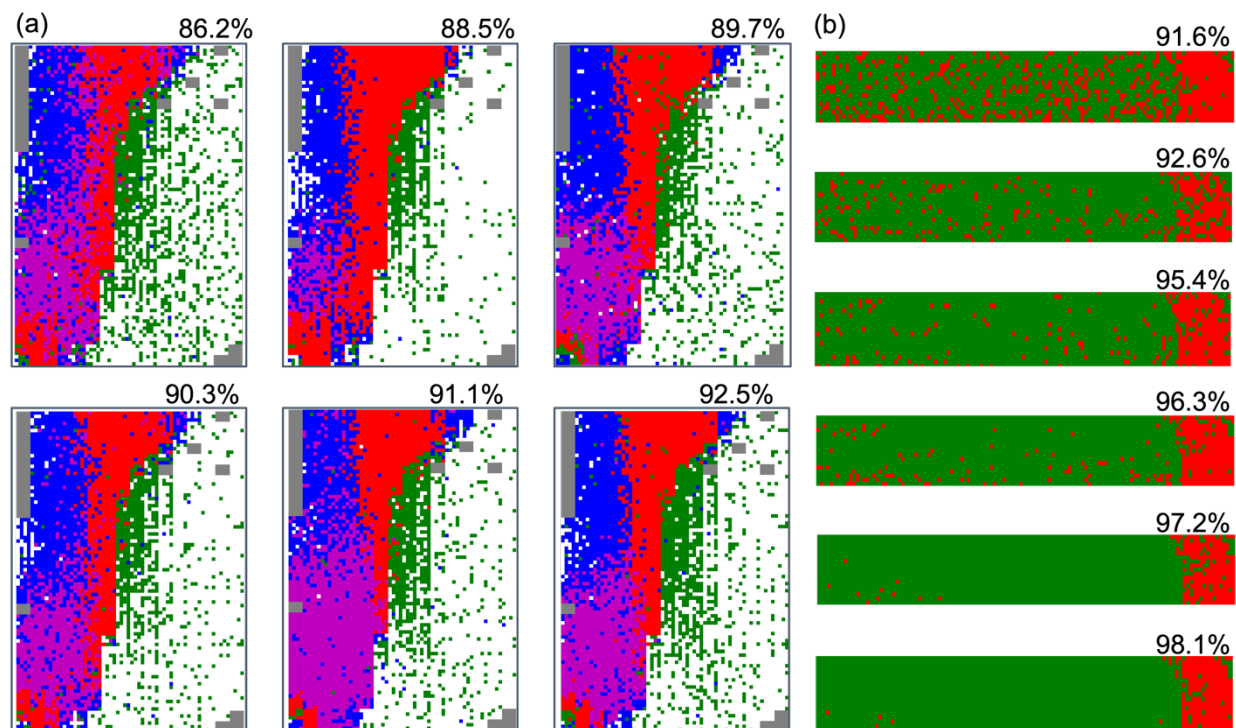


Figure 12 The predicted classes special distribution over the grid of SEM images. (a) the data for 425 °C with five distinct classes (b) the data for 500 °C sample with two distinct classes. The accuracy of prediction is given in %. The missing images on the grid are shown in gray.

Our s-GAN model classification based on ~ 5% of labeled images, selected randomly from data set, maps out to the five distinct zones as shown in Figure 12a. Typically, at least three major different microstructure zones are observed at joining region commonly referenced as a stir nugget zone (SN), a thermo-mechanically affected zone (TMAZ), and a heat affected zone (HAZ)

[5]. The microstructure of FSW zones depends on details of the tool design, the rotational and translational speeds and characteristics of the materials being joined. The tool and processing parameters are designed to heat working pieces just below the melting point to enable material flow and create welds with good mechanical properties. The stir nugget zone is the area trespassed by the rotating tool. This is the most severely deformed zone with dynamically recrystallized equiaxed micro grains, which are smaller than micro grains in other zones. The blue and magenta zones in Figure 12a correspond to the SN zone. The TMAZ zone reflects the effect of stirring close to the tool edge together with visible grain deformation due to material flow and local frictional heat. The effect of the tool shoulder is also evident in the broadening of this zone. Our model has mapped this zone in red (Figure 12a). The HAZ is also in the proximity of the tool edge. Its microstructure resembles the microstructure of the base material with elongated grain features but evident precipitates at the grain boundaries. This zone is mapped by the model as shown in green in Figure 12a. The white region in the same figure is dominated by the base material microstructural features. Data collected for the 500°C processed sample have revealed two distinct zones with apparent zone boundary obtained with higher accuracy models (Figure 12b). The zones correspond to the TMAZ mapped out in green and HAZ mapped out in red.

### 3.0 Conclusions

We studied correlation of processing parameters and microstructural features in friction stir welding (FSW) process. We presented novel approach for segmentation analysis of microstructures and deep learning semi supervised generative adversarial network s-GAN model for identifying the FSW zones without prior knowledge or empirical input about the zones. The benefits of our computational approach are threefold: First, Bayesian binning for determining segmentation thresholds enables automated analysis, which accurately estimates sizes, shapes, and number of prominent microstructural features. Second, the model allows mapping of the local residual deformation fields that are indicative of material flow and a likely indicator of residual stresses distribution over the cross-section of weld. Finally, the use of adversarial criterion in s-GAN model enables the generator to capture microstructural features implicitly and generate statistically equivalent synthetic images. At the same time, the discriminator model predicts the labeled classes trained with minimal amount of labeled data. The predicted classes map into empirically suggested FSW zones with an impressive performance. Developed methods and results have direct impact on the advancing the ability to establish quantitative PSPP relationships.

## 4.0 References

- [1] Computational Design of Hierarchically Structured Materials Science 277, 1237 (1997)  
G. B. Olson, et al. DOI: 10.1126/science.277.5330.1237
- [2] Rodgers, J.R., Cebon, D. Materials Informatics. MRS Bulletin 31, 975–980 (2006).
- [3] Surya R. Kalidindi, Stephen R. Niezgod, Ayman A. Salem Microstructure informatics using higher-order statistics and efficient data-mining protocols JOM, 63 (4) (2011), pp. 34-41
- [4] Bobby G. Sumpter, Sergei V. Kalinin, Richard K. Archibald Big-deep-smart data in imaging for guiding materials design Nat. Mater., 14 (2015), pp. 973-980
- [5] R. Nandan, T. DebRoy and H. K. D. H. Bhadeshia Recent Advances in Friction Stir Welding – Process, Weldment Structure and Properties Progress in Materials Science 53 (2008) 980-1023
- [6] R.S. Mishra, Z.Y. Ma Friction stir welding and processing Materials Science and Engineering R 50 (2005) 1–78
- [7] Thomas WM, Nicholas ED, Needham JC, Murch MG, Temple- Smith P, Dawes CJ (1991) Friction stir butt welding, International Patent Appl. No. PCT/GB92/02203 and GB Patent Appl. No. 9125978.8, December U.S. Patent No. 5460,317
- [8] P. J. Withers and H. K. D. H. Bhadeshia. Residual stress part 2 - nature and origins. Materials Science and Technology, 17:366–375, 2001.
- [9] P. S. Pao, S. J. Gill, C. R. Feng, and K. K. Sankaran. Corrosion-fatigue crack growth in friction stir welded Al 7050. Scripta Materialia, 45(5):605–612, 2001.
- [10] S. P. Donegan, J. C. Tucker, A. D. Rollett, K. Barmak, and M. Groeber. Extreme value analysis of tail departure from lognormality in experimental and simulated grain size distributions. Acta materialia, 61(15):5595-5604, 2013.
- [11] Arun M. Gokhale Quantitative Characterization and Representation of Global Microstructural Geometry ASM Handbook, Volume 9: Metallography and Microstructures G.F. Vander Voort, editor, p428–447 2004 DOI: 10.1361/asmhba0003759
- [12] W.B. Liewers, A.K. Pilkey An evaluation of global thresholding techniques for the automatic image segmentation of automotive aluminum sheet alloys Mater. Sci. Eng.: A, 381 (1) (2004), pp. 134-142
- [13] S.R. Niezgod, D.T. Fullwood, S.R. Kalidindi Delineation of the space of 2-point correlations in a composite material system Acta Mater., 56 (18) (2008), pp. 5285-5292
- [14] Brian L. DeCost, Elizabeth A. Holm A computer vision approach for automated analysis and classification of microstructural image data Comput. Mater. Sci., 110 (2015), pp. 126-133
- [15] Graham Roberts, Simon Y. Haile, Rajat Sainju, Danny J. Edwards, Brian Hutchinson and Yuanyuan Zhu Deep Learning for Semantic Segmentation of Defects in Advanced STEM Images of Steels Scientific Reports 9, 12744 (2019)

- [16] Chun, S., Roy, S., Nguyen, Y.T. et al. Deep learning for synthetic microstructure generation in a materials-by-design framework for heterogeneous energetic materials. *Scientific Reports* 10, 13307 (2020).
- [17] Seyed Majid Azimi, Dominik Britz, Michael Engstler, Mario Fritz, Frank Mücklich Advanced Steel Microstructural Classification by Deep Learning Methods *Scientific Reports* volume 8, Article number: 2128 (2018)
- [18] Steven R. Spurgeon, Colin Ophus, Lewys Jones, Amanda Petford-Long, Sergei V. Kalinin, Matthew J. Olszta, Rafal E. Dunin-Borkowski, Norman Salmon, Khalid Hattar, Wei-Chang D. Yang, Renu Sharma, Yingge Du, Ann Chiramonti, Haimei Zheng, Edgar C. Buck, Libor Kovarik, R. Lee Penn, Dongsheng Li, Xin Zhang, Mitsuhiro Murayama and Mitra L. Taheri Towards data-driven next-generation transmission electron microscopy *Nature Materials* 20, pages274–279 (2021)
- [19] Joseph Goldstein, Dale E. Newbury, David C. Joy, Charles E. Lyman, Patrick Echlin, Eric Lifshin, Linda Sawyer, J.R. Michael *Scanning Electron Microscopy and X-Ray Microanalysis*, Publisher Springer Nature 2018
- [20] Jeffrey D. Scargle, Jay P. Norris, Brad Jackson, and James Chiang Studies in astronomical time series analysis VI Bayesian blocks representations 2013 *The Astrophysical Journal* 764 167
- [21] Wei Li, Kevin G. Field and Dane Morgan Automated defect analysis in electron microscopic images, *npj Computational Materials* volume 4, Article number: 36 (2018)
- [22] Puja Shashi, Suchithra R, Review Study on Digital Image Processing and Segmentation *American Journal of Computer Science and Technology* 2, 4, 2019, Pages: 68-72
- [23] I. Goodfellow, J. Pouget-Abadie, M. Mirza, B. Xu, D. Warde-Farley, S. Ozair, A. Courville, and Y. Bengio. Generative adversarial nets. In *Advances in neural information processing systems*, pages 2672–2680, 2014
- [24] Augustus Odena Semi-Supervised Learning with Generative Adversarial Networks [arXiv:1606.01583](https://arxiv.org/abs/1606.01583)
- [25] Salimans, T., Goodfellow, I., Zaremba, W., Cheung, V., Radford, A., and Chen, X. Improved techniques for training gans. In *Advances in neural information processing systems*, pp. 2234–2242, 2016.
- [26] Abhishek Kumar, Prasanna Sattigeri, P. Thomas Fletcher Improved Semi-Supervised Learning with GANs using Manifold Invariances [arXiv:1705.08850](https://arxiv.org/abs/1705.08850)
- [27] Ross, Kenneth, Md Reza-E-Rabby, Martin McDonnell, and Scott A. Whalen. "Advances in dissimilar metals joining through temperature control of friction stir welding." *MRS Bulletin* 44, no. 8 (2019): 613-618.

## Appendix A – Supplementary Information

The details of s-GAN model architecture are shown in Figure 13.

Layer (type)	Output Shape	Param #
input_1 (InputLayer)	[(None, 256, 256, 1)]	0
conv2d (Conv2D)	(None, 128, 128, 24)	240
leaky_re_lu (LeakyReLU)	(None, 128, 128, 24)	0
conv2d_1 (Conv2D)	(None, 64, 64, 24)	5208
leaky_re_lu_1 (LeakyReLU)	(None, 64, 64, 24)	0
conv2d_2 (Conv2D)	(None, 32, 32, 24)	5208
leaky_re_lu_2 (LeakyReLU)	(None, 32, 32, 24)	0
conv2d_3 (Conv2D)	(None, 16, 16, 24)	5208
leaky_re_lu_3 (LeakyReLU)	(None, 16, 16, 24)	0
flatten (Flatten)	(None, 6144)	0
dropout (Dropout)	(None, 6144)	0
dense (Dense)	(None, 5)	30725
activation (Activation)	(None, 5)	0

Layer (type)	Output Shape	Param #
input_2 (InputLayer)	[(None, 384)]	0
dense_1 (Dense)	(None, 24576)	9461760
leaky_re_lu_4 (LeakyReLU)	(None, 24576)	0
reshape (Reshape)	(None, 32, 32, 24)	0
conv2d_transpose (Conv2DTran	(None, 64, 64, 24)	9240
leaky_re_lu_5 (LeakyReLU)	(None, 64, 64, 24)	0
conv2d_transpose_1 (Conv2DTr	(None, 128, 128, 24)	9240
leaky_re_lu_6 (LeakyReLU)	(None, 128, 128, 24)	0
conv2d_transpose_2 (Conv2DTr	(None, 256, 256, 24)	9240
leaky_re_lu_7 (LeakyReLU)	(None, 256, 256, 24)	0
conv2d_4 (Conv2D)	(None, 256, 256, 1)	24577

Figure 13 The s-GAN model architecture details a. generator model b. discriminator model

The grid points and corresponding low-resolution images at its points were shown in Figures 14 and 15 for 425 °C, and 500 °C samples respectively.

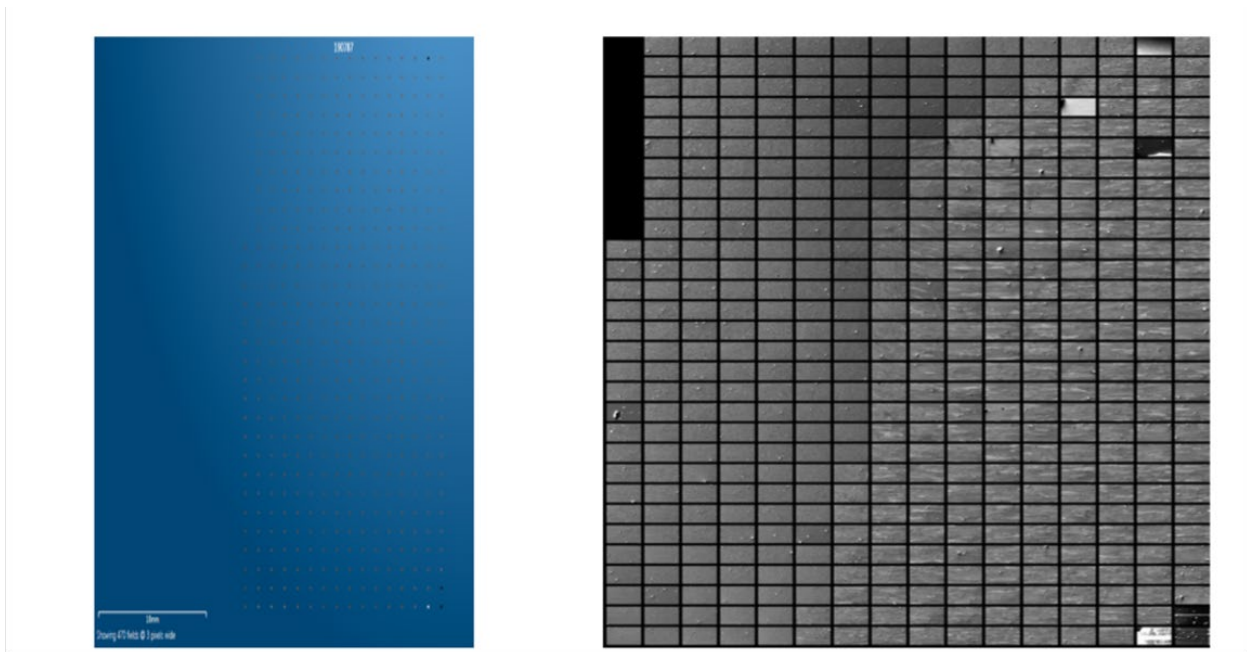


Figure 14 The summary of images taken at the cross section of FSW sample. The recorded temperature at the surface of weld sample was 425°C

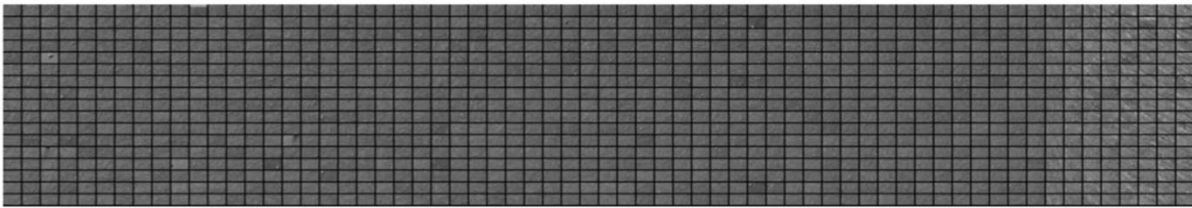
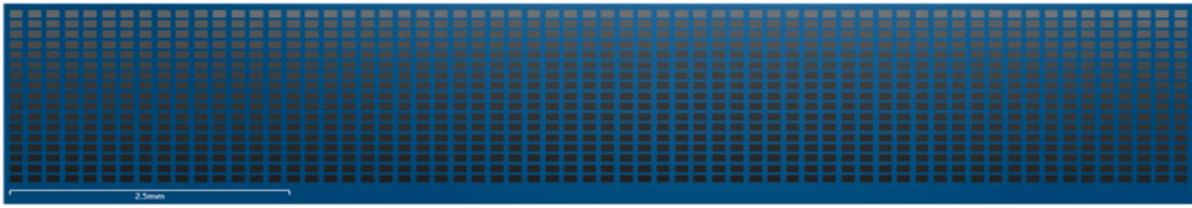


Figure 15 The summary of images taken at the cross section of FSW sample at the tool pin affected area. The recorded temperature at the surface of weld sample was 500°C.

# **Pacific Northwest National Laboratory**

902 Battelle Boulevard  
P.O. Box 999  
Richland, WA 99354  
1-888-375-PNNL (7665)

***[www.pnnl.gov](http://www.pnnl.gov)***